Correlation measurement of few-phonon interference

Yu Wang ,[1,2,5,*] Yan-Lei Zhang ,[1,2,5,*] Zhen Shen,[1,2,5,†] Hong-Yi Kuang,[1,2,3] Chang-Ling Zou,[1,2,5] Hui Jing,[3]
Yun-Feng Xiao,[4,5] Guang-Can Guo,[1,2,5] and Chun-Hua Dong [1,2,5,‡]

[1] *CAS Key Laboratory of Quantum Information, University of Science and Technology of China, Hefei, Anhui 230026, China*
[2] *CAS Center for Excellence in Quantum Information and Quantum Physics, University of Science and Technology of China, Hefei, Anhui 230088, China*
[3] *Key Laboratory of Low-Dimensional Quantum Structures and Quantum Control of Ministry of Education, Department of Physics and Synergetic Innovation Center for Quantum Effects and Applications, Hunan Normal University, Changsha 410081, China*
[4] *State Key Laboratory for Mesoscopic Physics and Frontiers Science Center for Nano-optoelectronics, School of Physics, Peking University, Beijing 100871, China*
[5] *Hefei National Laboratory, University of Science and Technology of China, Hefei, Anhui 230088, China*

(Received 1 September 2023; revised 30 November 2023; accepted 5 March 2024; published 21 March 2024)

The interferometer is a vital technology in achieving coherent control and measurement in quantum systems. In this study, we present a few-phonon interferometer based on an optomechanical crystal cavity, which is cooled down with several phonons even less. Through the phonon counting, the competition between the thermal and coherent phonons is demonstrated by the interference. The interference visibility is monotonically increased with increasing the coherent phonons. However, the interference on second-order correlation $g^{(2)}(0)$ occurs in reverse because of the different statistical properties of thermal and coherent phonons, which also leads to an unnatural interference visibility with great coherent phonons. The investigation of this correlation interference technology will advance the development of cavity optomechanics systems in the quantum precision sensing and quantum information processing fields.

DOI: 10.1103/PhysRevA.109.033523

I. INTRODUCTION

The interference method of separated oscillating fields can produce atomic and molecular transition frequencies with unrivaled precision and accuracy [1,2]. Several remarkable applications have been reported, ranging from atomic frequency standards [3–6] and Bose-Einstein condensates [7], to quantum information processing [8–12] and the study of phase coherence in two-level systems [13,14]. In recent years, this method has been extended to investigate mechanical motion degrees of freedom [15–18]. This is mainly due to the increasing role of cavity optomechanics in precision measurement [19–23], frequency conversion [24,25], topological lattice [26], quantum entanglement [27,28], and mesoscopic quantum state engineering [29–31]. As the interference fringe is sensitive to the dynamical changes of mechanical state in the phase, phonon interferometry is an important technology for detecting the dynamic processes of optomechanical systems.

In the previous optomechanical interferometer [16], the population of coherent phonons was large, and the interference fringes were obtained by using heterodyne detection without considering thermal phonons, which would directly participate and influence the interference. To explore the interferometer under the influence of few thermal phonons, an alternative method is correlation measurement based on photon counting, as intensity correlations provide statistic information that is not available from the measurements of first-order coherence. This approach has been not only used for astronomical research of thermal light using Hanbury Brown–Twiss (HBT) technology [32,33], but also for early research on photon statistics of lasers and resonance fluorescence [34,35]. The introduction of photon counting and correlation measurement will promote the use of phonon interferometer for coherent control and detection of quantum cavity optomechanical systems.

Here, we have demonstrated few-phonon interferometer using an optomechanical crystal (OMC) nanobeam cavity, which is placed in a cryostat and cooled down with several phonons even less. The interference fringes of phonons are observed using photon counting and second-order correlation. And the interference visibility of the former is monotonically increased with increasing the coherent phonons. However, the interference on second-order correlation $g^{(2)}(0)$ exhibits a π phase shift because of the different statistical properties of thermal and coherent phonons, which also leads to a decreasing interference visibility with great coherent phonons. The research of this single phonon level interference technology will promote the application of cavity optomechanics systems in quantum precision sensing and quantum information processing.

II. THEORY

In the phonon interferometry, two pairs of pulses with separation time T, including the drive and probe fields, are

*These authors contributed equally to this work.
†shenzhen@ustc.edu.cn
‡chunhua@ustc.edu.cn

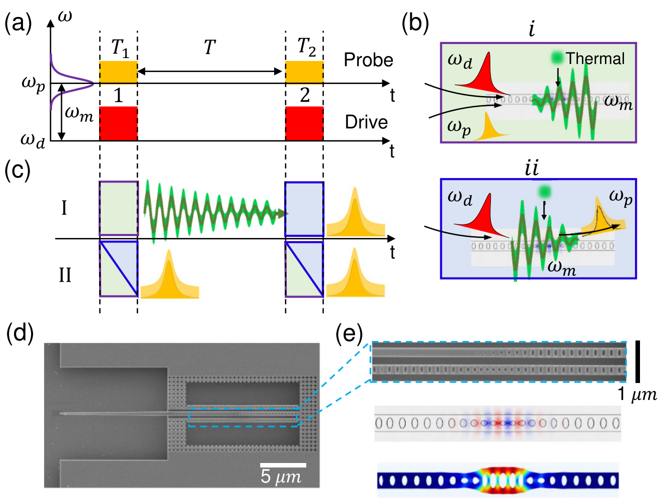

FIG. 1. (a) The spectral diagram and pulse sequences of the phonon interferometry. (b) The drive field converts the probe photons to coherent phonons in the presence of the mechanical thermal bath (i), and meanwhile serves as a parametric source to up-convert a phonon, including the thermal phonon occupation, into the cavity resonance (ii). (c) The phonon interference can be verified by the scattered photons by the residual phonons from pulse 1 (I) and the regenerated phonons from pulse 2 (II). The color code corresponds to the interaction diagrams involved in these two paths. (d) Scanning electron microscope (SEM) image of the OMC device. (e) SEM image of an individual nanobeam OMC and the coupling waveguide (top), finite-element method simulations of the optical field (middle) and mechanical displacement profile (bottom).

sent to the optomechanical cavity, as shown in Fig. 1(a). When the drive field (ω_d) is red-detuned from the optical mode (ω_c) by one mechanical frequency ω_m, the effective Hamiltonian of the system with the weak probe laser (ω_p) is

$$H_\mathrm{eff} = \Delta(c^\dagger c + m^\dagger m) + G(c^\dagger m + cm^\dagger) + i\sqrt{\kappa_\mathrm{ex}}\varepsilon_\mathrm{p} c^\dagger + i\sqrt{\gamma_\mathrm{m}} m_\mathrm{th} m^\dagger + \mathrm{H.c.}, \quad (1)$$

where $\Delta = \omega_\mathrm{c} - \omega_\mathrm{p}$, and c ($c^\dagger$) and m ($m^\dagger$) are annihilation (creation) operators for the optical and mechanical mode, respectively. $G = g_0\sqrt{n_\mathrm{d}}$ is the optomechanical coupling rate, which is enhanced via the intracavity photon number n_d from the drive laser. ε_p is the amplitude of the probe laser with the coupling rate κ_ex. Different from the coherent state of the probe laser, the mechanical mode with the decay rate of γ_m is motivated by the thermal noise m_th. It is noticed that the phonon interference is affected by the competition between the coherent phonon and the thermal phonon, which is the fundamental difference from the traditional interference process that is only determined by the detuning Δ and the separation time T.

To provide a more intuitive explanation of the entire process, the interaction diagram is plotted in Fig. 1(b). The well-known photon–phonon coherent conversion occurs via a beam-splitter-like interaction [36,37], resulting in two processes during the pulse pair: (i) the drive field converts the probe photons to coherent phonons in the presence of the thermal bath through the mechanical interaction, and (ii) the drive field served as a parametric source upconvert a phonon, including the thermal phonon occupation, into the cavity resonance. During the first pulse, these two processes will produce coherent phonon occupancy and cavity photons with thermal noise. The cavity photons decay quickly to zero during the free evolution, while the mechanical excitations have almost no decay except for accumulating an additional phase $\omega_\mathrm{m} T$ until the second pulse arrives, since the decay time $1/\gamma_\mathrm{m}$ is longer than T and the decay time of photon (see Appendixes). The cavity photons interference during pulse 2 consists of two parts, one scattered by the residual phonons from pulse 1 (I), and others scattered by the regenerated phonons from pulse 2 (II), as shown in Fig. 1(c). Therefore, the interference fringes observed in the optical domain represent the interference between phonons created by pulse 1 and 2. It is worth noting that two probe pulses cannot interfere directly as the free evolution time is much longer than the optical decay time. Meanwhile, the participation of the thermal phonon will affect the interference visibility of the phonon interferometry, which is also distinguished from the direct interference of coherent light.

The dynamics of the optomechanical system can be described by the following equations:

$$\frac{dc}{dt} = -\left(\frac{\kappa_\mathrm{c}}{2} + i\Delta\right)c - iG(t)m + \sqrt{\kappa_\mathrm{ex}}\varepsilon_\mathrm{p},$$
$$\frac{dm}{dt} = -\left(\frac{\gamma_\mathrm{m}}{2} + i\Delta\right)m - iG(t)c + \sqrt{\gamma_\mathrm{m}} m_\mathrm{th}, \quad (2)$$

where κ_c is the decay rate of the optical mode. When two pairs of pulses meet with the separation time T, the mechanical field can be solved as

$$m = \sqrt{n_\mathrm{th}}\frac{m_\mathrm{th}}{|m_\mathrm{th}|} + \sqrt{n_\mathrm{coh1}}e^{i\varphi_1}\frac{\varepsilon_\mathrm{p,1}}{|\varepsilon_\mathrm{p,1}|} + \sqrt{n_\mathrm{coh2}}e^{i\varphi_2}\frac{\varepsilon_\mathrm{p,2}}{|\varepsilon_\mathrm{p,2}|},$$

which is decomposed into the thermal phonon occupation (n_th) and coherent phonon population $n_\mathrm{coh1(2)}$ created by pulse 1 (2), respectively. The coherent phonons decay with time, showing Lorentzian-like response in the frequency distribution (see Appendixes). Additionally, our detection cannot distinguish n_th with different frequencies. Therefore, all frequency of thermal phonon population should be considered when calibrating n_th at any ω_p. For the sake of simplicity, we still depict this integral mean thermal phonon occupation $\int_{\omega_\mathrm{p}} n_\mathrm{th} d\omega_\mathrm{p}$ as n_th in the following description. Therefore, the mean phonon occupation of the system can be written as

$$\langle m^\dagger m\rangle = n_\mathrm{th} + n_\mathrm{coh1} + n_\mathrm{coh2} + 2\sqrt{n_\mathrm{coh1}n_\mathrm{coh2}}\cos(\delta), \quad (3)$$

where the last term represents the interference of coherent phonons with different phases, i.e., $\delta = \varphi_1 - \varphi_2$. The $\cos(\delta)$ is approximately $\cos(\Delta T)$ for the short enough pulse 2 but not involve n_th due to its disordered phase. According to the input-output theory, when it is near critical coupling, the field reflected from the resonator is $c_\mathrm{out} \approx -i\sqrt{\kappa_\mathrm{ex}P_\mathrm{s}}m$, where P_s represents the scattering probability of a phonon to a photon. Thus the output photons can be used for the detection of the interference fringes of phonons described above. From Eq. (3), we find that the phonon interference is attributed to the coherent phonons, and the thermal phonons weaken the interference. Especially, there is no oscillation for the disordered phase of the thermal noise when $n_\mathrm{coh} = n_\mathrm{coh1} + n_\mathrm{coh2} + 2\sqrt{n_\mathrm{coh1}n_\mathrm{coh2}}\cos(\delta) \ll n_\mathrm{th}$. However, the measurement of light intensity can only reflect the difference between the thermal and coherent phonons, and the nonclassical states are even more impossible to distinguish from the coherent states.

The second-order correlation of the phonons can be calculated as

$$g^{(2)}(\tau) = \frac{m^\dagger(0)m^\dagger(\tau)m(\tau)m(0)\rangle}{\langle m^\dagger(0)m(0)\rangle^2},$$

which can be mapped by the second-order correlation of the output photons. Here, we measure $g^{(2)}(0)$, which can be derived as

$$g^{(2)}(0) \approx 2 - \frac{1}{(1 + n_{\text{th}}/n_{\text{coh}})^2}. \tag{4}$$

It shows the correlation interference fringes $1 \leqslant g^{(2)}(0) \leqslant 2$, where $g^{(2)}(0) = 1(2)$ is corresponding to the condition $n_{\text{th(coh)}} = 0$. This originates from the statistical properties of the thermal bath and coherent field. By combining first- and second-order correlations, we can simultaneously obtain the information of both $n_{\text{th}} + n_{\text{coh}}$ and $n_{\text{th}}/n_{\text{coh}}$, which are ideally suitable for $n_{\text{th}} \approx n_{\text{coh}}$. More importantly, the second-order correlation of the phonon interference can show huge advantages, where its value oscillates wildly for the nonclassical states $g^{(2)} \gg 1$ or $\ll 1$, and the method is expected to greatly promote the application in the field of quantum precision sensing.

III. EXPERIMENTAL RESULT

To obtain the phonon interferometry, a nanobeam OMC cavity [38] is used here, as shown in Fig. 1(d). Finite-element method numerical simulations of the optical E_y field and mechanical displacement field are shown in Fig. 1(e). The device uses one-dimensional (1D) periodically arranged Si nominal unit cells to create high-Q colocalized optical and mechanical resonances [38,39]. Independent measurements are initially performed in a dilution refrigerator ($\approx$10 mK) to characterize the optical and mechanical modes and the optomechanical coupling rate [40]. A tunable laser is coupled into the silicon waveguide via a lensed optical fiber, as shown in Fig. 2(a). Then, the signal is reflected from the on-chip waveguide via a high-reflectivity photonic crystal end-mirror and measured through the detector (not shown here) using the circulator. For the device under test in this work, an optical resonance ω_c at a wavelength of 1533.87 nm has a decay rate of $\kappa_c/2\pi = 886$ MHz, corresponding to optical quality factor $Q_o \approx 220\,000$, as shown in Fig. 2(b). Figure 2(c) shows the thermal mechanical spectrum of the breathing mode exhibits a Lorentzian profile.

For the experiment, the AOM is used to generate drive pulses with the desired duration and timing [41]. An additional prefilter following the laser is used to remove the phase noise of our driving field at mechanical frequency [42]. The probe pulses are the blue sideband of the drive pulses, which are generated by the EOM. The output pulse pairs pass through the cascaded filters to remove the driving field and then launched into a HBT-type setup which comprised of a 50 : 50 fiber splitter and two SNSPDs [43]. Therefore, with a lot of repeated pulse sequences, statistics on the single-photon count rates and intensity correlation of signal photons

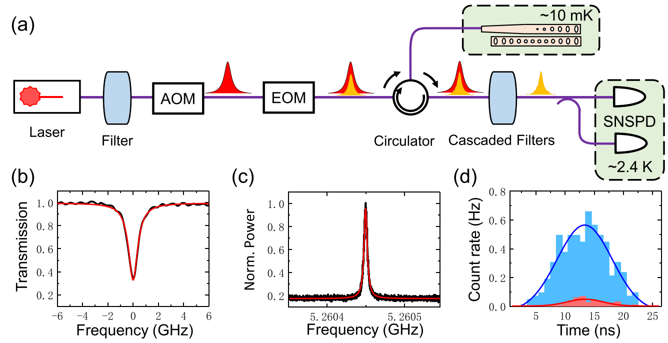

FIG. 2. (a) Schematic of the experimental setup. AOM, acousto-optic modulator; EOM, electro-optic modulator; SNSPD, superconducting nanowire single-photon detector. (b) Transmission spectrum for the optical resonance around 1533 nm. (c) Optically transduced thermal mechanical spectrum of the breathing mode with $\omega_m/2\pi = 5.26$ GHz and $\gamma_m/2\pi = 5$ kHz. (d) Sideband thermometry to extract the thermal occupation of the mechanical resonator. n_{th} is estimated as 0.071 ± 0.008.

in second pulse are performed, indicating the results of the phonons. First, the cavity-enhanced Stokes (blue sideband) and anti-Stokes (red sideband) scattering rates are measured to obtain the actual thermal occupation of the mechanical mode when the cavity is excited by a sequence of alternating blue- or red-detuned optical pulses ($\approx\omega_c \pm \omega_m$) with a duration of 40 ns [39]. Figure 2(d) shows a histogram of the respective single-photon count rates with a peak power of 0.67 μW for $\approx$50 hours. The frequency of the drive pulses is locked to a wave meter. We extract a thermal occupation of $n_{\text{th}} = 0.071 \pm 0.008$, which is also used for the calibration of the phonon population in the system. Figure 3(a) shows the single-photon count rates measured during pulse 2 as a function of detuning Δ and the separation time T. Here, the first pulse pair ($T_1 = 4$ μs) excites the initial coherent phonon occupations $n_{\text{coh1}} = 15.7$ at $\Delta = 0$, $t = T_1 + 5$ μs and

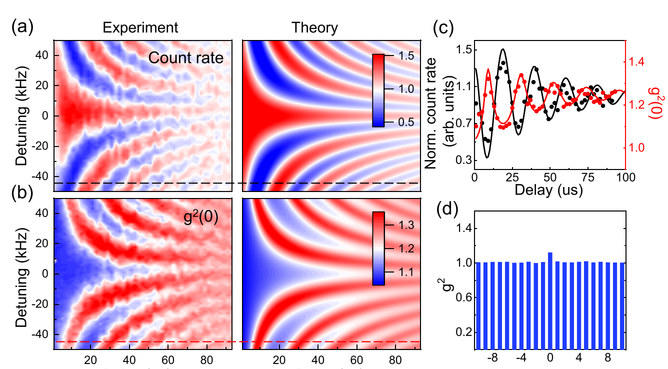

FIG. 3. (a), (b) Experimental and theoretical normalized single-photon count rates (a) and $g^{(2)}(0)$ (b) measured during pulse 2 as a function of Δ and T with $T_1 = 4$ μs and $T_2 = 0.4$ μs. (c) Interference oscillations versus the separation time at $\Delta = -45$ kHz, as shown the dot lines in panels (a) and (b). (d) The typical correlations between coinciding detection events on the SNSPDs for photons emerging with different pulse sequences. Δ and T are -11 kHz and 23 μs, respectively.

thermal noise $n_{\rm th} = 12.89$ due to residual heat through laser absorption (see Appendix B 2 for calibration). The duration of the second pulse pair is chosen as $T_2 = 0.4$ μs to reduce the heating. The peak power in the waveguide of drive pulses (1 and 2) is 2.1 μW, and the repetition rate of the pulse pairs is 5 kHz. The photon count rates are normalized to the value of $(I_{\rm max} + I_{\rm min})/2$, where $I_{\rm max}$ ($I_{\rm min}$) is the maximum (minimum) count rate of the interference fringe. The distinct spectral oscillations observed in Fig. 3(a) demonstrate the fringe for the OMC cavity. Figure 3(b) plots the phonon correlation $g^{(2)}(0)$ at the same pulse sequence in Fig. 3(a) through the HBT-type setup. For a mechanical resonator transition from a purely thermal state into a displaced thermal state, the phonon intensity correlation at $\tau = 0$ will change from bunching $[g^{(2)}(0) = 2]$ to Poissonian statistics $[g^{(2)}(0) = 1]$. Because of the phonon interference, the coherent phonon occupancy $n_{\rm coh}$ (and $n_{\rm coh}/n_{\rm th}$) will oscillate with the detuning Δ and separation time T, demonstrating the phonon interferometry based on phonon intensity correlations. Since the destructive (constructive) interference on the single-photon count rates is attributed to the smaller (larger) coherent component, the corresponding $g^{(2)}(0)$ is closer to bunching (Poissonian statistics). Therefore, the fringes on $g^{(2)}(0)$ are generally the opposite of that on single-photon count rates, for example, as shown in Fig. 3(c), which are the horizontal cuts indicated in Figs. 3(a) and 3(b) (black and red dashed lines). In addition, the decay of this interference can extract the decoherence lifetime $\tau_2 = 19.9$ μs by theoretically fitting with an exponentially decaying sine-liked function which is approximated to Eq. (3) (see Appendixes).

Using the HBT-type setup, we detect the second-order correlation $g^{(2)}(\Delta N)$ of the scattered photons from pulse 2, which refers to the coincidences between detection events originating from the same ($\Delta N = 0$) or different ($\Delta N \neq 0$) pulse sequences, as shown in Fig. 3(d). The ΔN here is the relative sequence number difference of clicks from the two SNSPDs in a large number of independent identically distributed experiments. For the same ($\Delta N = 0$) pulse sequences, the scattered signal photons show the same statistical properties as phonons, which comprise of thermal $[g^{(2)}(0) = 2]$ and coherent $[g^{(2)}(0) = 1]$ ones. Based on Eq. (4), the value of $g^{(2)}(0)$ is determined by the ratio $n_{\rm coh}/n_{\rm th}$. This oscillatory signature in Fig. 3(b) will become nonobvious if $n_{\rm coh} \gg n_{\rm th}$, thus the characterization is limited when ignoring the thermal occupation in previous work [16].

The decoherence of a massive object, such as phonons, is influenced by the interaction with a thermal bath. Figure 4(a) shows the normalized count rates with various coherent phonon occupations $n_{\rm coh}$. The thermal noise is fixed as $n_{\rm th} = 12.89$ and $n_{\rm coh}$ is controlled by changing the modulation power of the EOM. The oscillation of the interferometer on count rate is decreased with decreasing the coherent phonons and still obvious when $n_{\rm coh} = 0.39$. In addition, $g^{(2)}(0)$ with various $n_{\rm coh}$ is shown in Fig. 4(b). Note that the oscillation is stronger with less coherent phonons, which is different from the previous results. Therefore, we extract the interference visibility from the interference spectra versus $n_{\rm coh}/n_{\rm th}$, as shown in Figs. 4(c) and 4(d). Note that the interference visibility $V_{\rm count}$ from the single-photon count rates gradually increases with the ratio $n_{\rm coh}/n_{\rm th}$ increasing, then almost reaches the

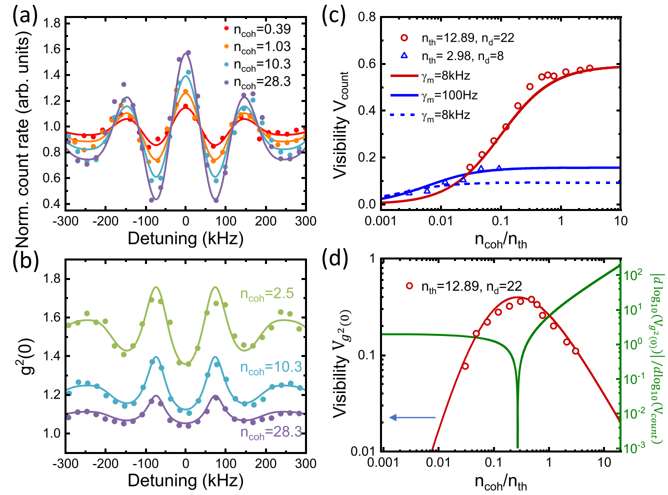

FIG. 4. (a), (b) Normalized single-photon count rates and $g^{(2)}(0)$ as a function of detuning Δ for various $n_{\rm coh}$ with $n_{\rm th} = 12.89$ and $n_{\rm d} = 22$. (c), (d) Interference visibility of the interference fringes as a function of $n_{\rm coh}/n_{\rm th}$ for count rates and $g^{(2)}(0)$. The solid lines in panels (a)–(d) indicate theoretically expected values. The dashed lines in panel (c) show the theoretical results with the fixed decay rate. The green line in panel (d) shows the calculated ratio of $|{\rm d}\log_{10}(V_{g^{(2)}(0)})|/{\rm d}\log_{10}(V_{\rm count})$.

maximum and saturates, which is in line with physical intuition and previous results for $n_{\rm coh} \gg n_{\rm th}$ [16]. In other words, a saturation trend appears when coherent phonon occupation reaches a level at which the influence of thermal occupation becomes negligible. When the drive peak power is reduced from 2.1 to 0.67 μW and the pulse repetition rate is reduced to 50 Hz to get the lower thermal occupation ($n_{\rm th} = 2.98$), the interference visibility is around 0.1 when the coherent phonon occupation is as low as 0.12, as shown the blue line in Fig. 4(c). Both curves have similar characteristics, where saturation point and maximum value are determined by $\gamma_{\rm m}$ and $n_{\rm d}$ for a given pulse timing and a determined device (see Appendixes). It is worth noting that the solid lines in Fig. 4(c) represent the theoretically expected values using the parameters $\gamma_{\rm m} \approx 8$ kHz and 100 Hz when $n_{\rm th} = 12.89$ and 2.98, respectively, while the dashed line shows the deviation results using $\gamma_{\rm m} \approx 8$ kHz for $n_{\rm th} = 2.98$. This decreased $\gamma_{\rm m}$ with small $n_{\rm th}$ can be intuitively interpreted by two-level system interactions [30] and the thermal decoherence processes [20].

A stronger drive can enhance the optomechanical interaction and improve the probability of photon-phonon conversion, resulting in a larger interference visibility. On the contrary, it can be seen the interference visibility from $g^{(2)}(0)$ decreases quickly when $n_{\rm coh}/n_{\rm th} \gg 1$, indicating the statistical property of the mechanical resonator tends to be a stable Poisson distribution. Meanwhile, for $n_{\rm coh}/n_{\rm th} \ll 1$, $V_{g^{(2)}(0)}$ also decreases because the statistical property of the mechanical resonator tends to be a pure thermal distribution. Therefore, there is a maximum value of interference visibility, in this case, located near $n_{\rm coh}/n_{\rm th} \approx 0.4$. This correlation phonon interference allows us to extract the thermal phonon population, especially in the case of large numbers of coherent phonons, due to the distinguishable interference visibility of $g^{(2)}(0)$ in this region ($n_{\rm coh}/n_{\rm th} \gg 1$), where $V_{\rm count}$

is almost saturated. As shown green line in Fig. 4(d), the ratio $|d\log_{10}(V_{g^{(2)}(0)})|/d\log_{10}(V_{\rm count})$ can be as high as 200. This correlation phonon interference allows us to assess the effect of thermal phonons or other possible nonclassical states by the interference visibility.

In summary, we have implemented a phonon interferometer at the single-phonon level in an optomechanical resonator and characterized the interference fringes through first- and second-order correlation in the presence of the thermal bath, which influences the visibility of interference fringes. The saturation trend of interference visibility of phonon population provides a way to set an optimal work point of $n_{\rm coh}/n_{\rm th}$ with more obvious interference fringes, and the unnatural interference visibility changes of $g^{(2)}(0)$ can be used to calibrate the thermal phonons. As our scheme involves both coherent and thermal phonons, and the evolution of this kind of mixed state, it is appropriate to study the thermal dynamical decoherence processes of phonons. Our results not only establish the groundwork for applying phonon interferometry technology to quantum optomechanical systems, but also enable applications such as phonon occupation sensing, exploration of dynamical interactions between mechanical oscillators, and the thermal dynamical decoherence processes of phonons.

ACKNOWLEDGMENTS

The authors thank M. Zhang for helpful discussions. This work was supported by the National Key Research and Development Program of China (Grant No. 2020YFB2205801), Innovation program for Quantum Science and Technology (2021ZD0303203), National Natural Science Foundation of China (Grants No. 12293052, No. 11654003, No. 11934012, No. 12104442, No. 92050109, No. 92250302, No. U21A20433, and No. 92265108), the Natural Science Foundation of Anhui Province (Grants No. 2108085MA17 and No. 2308085J12), the CAS Project for Young Scientists in Basic Research (YSBR-069), and the Fundamental Research Funds for the Central Universities. This work was partially carried out at the USTC Center for Micro and Nanoscale Research and Fabrication.

APPENDIX A: THEORY

1. Model

As discussed in the main text, we consider a general optomechanical system in the resolved-sideband limit. Under the strong driving pump $\epsilon_{\rm d}$ with the red detuning, the optomechanical system can be linearized as the coherent interaction $G(c^\dagger m + cm^\dagger)$ with the coupling strength $G = g_{\rm o}\sqrt{n_{\rm d}}$, where $g_{\rm o}$ indicates the single-photon optomechanical coupling rate and

$$n_{\rm d} = \frac{\kappa_{\rm ex}|\epsilon_{\rm d}|^2}{\Delta^2 + \kappa_{\rm c}^2/4}$$

is the average photon number in the intracavity field from the pump laser [20]. Here we study the dynamical evolution of the optomechanical system, and a probe field weaker than the driving pump is used to stimulate the system [36]. In the rotating frame $H_{\rm o} = \omega_{\rm p} c^\dagger c + (\omega_{\rm p} - \omega_{\rm d}) m^\dagger m$, the corresponding Hamiltonian can be written as

$$\begin{aligned} H = {} & (\omega_{\rm c} - \omega_{\rm p}) c^\dagger c + (\omega_{\rm m} + \omega_{\rm d} - \omega_{\rm p}) m^\dagger m \\ & + G(c^\dagger m + cm^\dagger) + i\sqrt{\kappa_{\rm ex}}(c^\dagger c_{\rm in} - cc_{\rm in}^*) \\ & + ic_{\rm noise}\sqrt{\kappa_{\rm o}}(c^\dagger c_{\rm noise} - cc_{\rm noise}^*) \\ & + im_{\rm th}\sqrt{\gamma_{\rm m}}(m^\dagger m_{\rm th} - mm_{\rm th}^*), \end{aligned} \tag{A1}$$

where c ($c^\dagger$) and m ($m^\dagger$) are annihilation (creation) operators for the optical and mechanical resonator modes with the frequencies $\omega_{\rm c}$ and $\omega_{\rm m}$, respectively, and $\omega_{\rm d}$ ($\omega_{\rm p}$) is the frequency of the pump (probe) laser. In addition to considering the probe signal $c_{\rm in}$ with the coupling rate $\kappa_{\rm ex}$, we also need to consider the optical noise $c_{\rm noise}$ with the intrinsic rate $\kappa_{\rm o}$ and the mechanical thermal bath $m_{\rm th}$ with the intrinsic dissipative coupling rate $\gamma_{\rm m}$, and we notice that the mechanical thermal noise depends on the ambient temperature. Therefore, the dynamical evolution of the optomechanical system can be described by the following equations:

$$\frac{dc}{dt} = -\left[\frac{\kappa_{\rm c}}{2} + i(\omega_{\rm c} - \omega_{\rm p})\right]c - iGm + \sqrt{\kappa_{\rm ex}}c_{\rm in} + \sqrt{\kappa_{\rm o}}c_{\rm noise}, \tag{A2}$$

$$\frac{dm}{dt} = -\left[\frac{\gamma_{\rm m}}{2} + i(\omega_{\rm m} + \omega_{\rm d} - \omega_{\rm p})\right]m - iGc + \sqrt{\gamma_{\rm m}}m_{\rm th}, \tag{A3}$$

where we have assumed the red detuning $\omega_{\rm c} = \omega_{\rm m} + \omega_{\rm d}$ and defined $\Delta = \omega_{\rm c} - \omega_{\rm p} = \omega_{\rm m} + \omega_{\rm d} - \omega_{\rm p}$, and $\kappa_{\rm c} = \kappa_{\rm ex} + \kappa_{\rm o}$ is the total dissipative rate. In our experiment, we want to investigate the phonon process, which is a dynamical evolution driven by pulsed lasers. Therefore, the optomechanical system is not in a steady state. To study the dynamical evolution of the system in this case, we seek the analytical solutions of the equations. By defining the evolution rates, $A = \frac{\kappa_{\rm c}}{2} + i\Delta$, $B = \frac{\gamma_{\rm m}}{2} + i\Delta$, and the input signals, $A_{\rm in} = \sqrt{\kappa_{\rm ex}}c_{\rm in} + \sqrt{\kappa_{\rm o}}c_{\rm noise}$, $B_{\rm in} = \sqrt{\gamma_{\rm m}}m_{\rm th}$, the dynamical equations can be written as

$$\frac{dc}{dt} = -Ac - iGm + A_{\rm in}, \tag{A4}$$

$$\frac{dm}{dt} = -Bm - iGc + B_{\rm in}. \tag{A5}$$

We know that this set of equations has the general solutions:

$$c = A_1 \exp(x_1 t) + A_2 \exp(x_2 t) + A_0, \tag{A6}$$

$$m = B_1 \exp(x_1 t) + B_2 \exp(x_2 t) + B_0, \tag{A7}$$

where the exponential coefficients of the general solution are

$$\begin{aligned} x_1 &= \frac{-(A+B) + \sqrt{(A-B)^2 - 4G^2}}{2}, \\ x_2 &= \frac{-(A+B) - \sqrt{(A-B)^2 - 4G^2}}{2}. \end{aligned} \tag{A8}$$

x_1 represents a relatively slow decay rate with the parameter $4G^2 < (A - B)$ in our experiment. However, x_2 is the quick decay rate, and the corresponding term can be neglected if $|x_2|t \gg 1$. When the system is in the steady state, we have the solutions

$$A_0 = -\frac{iGB_{\text{in}} - BA_{\text{in}}}{(AB + G^2)}, \quad B_0 = -\frac{iGA_{\text{in}} - AB_{\text{in}}}{(AB + G^2)}, \tag{A9}$$

which depend on the input signals A_{in} (B_{in}) and have nothing with the initial state. For the dynamical process, the evolution also depends on the initial values $c(0)$ and $m(0)$, and the corresponding parameters, the amplitudes of terms that evolve rapidly (slowly) with time, A_1 and B_1 (A_2 and B_2), are

$$A_1 = \frac{c'(0)x_1 - x_1x_2[c(0) - A_0]}{x_1^2 - x_1x_2},$$

$$A_2 = \frac{c'(0)x_2 - x_1x_2[c(0) - A_0]}{x_2^2 - x_1x_2}, \tag{A10}$$

$$B_1 = \frac{m'(0)x_1 - x_1x_2[m(0) - B_0]}{x_1^2 - x_1x_2},$$

$$B_2 = \frac{m'(0)x_2 - x_1x_2[m(0) - B_0]}{x_2^2 - x_1x_2}, \tag{A11}$$

where $c'(0)$ and $m'(0)$ are initial values for taking the first derivative of time, which can be written as

$$c'(0) = -Ac(0) - iGm(0) + A_{\text{in}}, \tag{A12}$$

$$m'(0) = -Bm(0) - iGc(0) + B_{\text{in}}, \tag{A13}$$

which are determined by the initial states and the input signals.

Therefore, we can obtain the analytical results, and the dynamical process can be clearly described. These results are suitable for any input signal, including the coherent state, the thermal noise, or the nonclassical state. In addition, the dynamical evolution is established for any initial state, so the evolution of the segments can also be accurately described. Besides the evolution of the field intensity, we can also calculate the statistical property of the field to distinguish the coherent, thermal, and other states if we know the statistical properties of the input signals and initial states. In conclusion, the amplitude, phase, and statistical properties of the intracavity or extracavity field can be obtained by analytical solutions.

The noise correlators associated with the input fluctuations are given by [20]

$$\langle c_{\text{noise}}^\dagger c_{\text{noise}}\rangle = 0, \quad \langle c_{\text{noise}} c_{\text{noise}}^\dagger\rangle = 1, \tag{A14}$$

$$\langle m_{\text{th}}^\dagger m_{\text{th}}\rangle = n_{\text{m}}, \quad \langle m_{\text{th}} m_{\text{th}}^\dagger\rangle = n_{\text{m}} + 1. \tag{A15}$$

Therefore, in this model, we can ignore the noise of the optical mode, since $\langle c_{\text{noise}}^\dagger c_{\text{noise}}\rangle = 0$ and the theoretical derivation in this model does not involve the item $\langle c_{\text{noise}} c_{\text{noise}}^\dagger\rangle$. However, the noise of the mechanical mode cannot be neglected while

$$n_{\text{m}} = \frac{1}{e^{\hbar\omega_{\text{m}}/k_B T} - 1} \neq 0,$$

which represents the equivalent phonon occupation of mechanical mode corresponding to the ambient thermal bath [20]. From the above expressions, Eq. (A7) can be reorganized into

$$m = \sqrt{n_{\text{coh}}}\frac{c_{\text{in}}}{|c_{\text{in}}|} + \sqrt{n_{\text{th}}}\frac{m_{\text{th}}}{|m_{\text{th}}|}, \tag{A16}$$

which means that the mechanical motion of the optomechanical system is comprised of the coherent component transformed from the probe field c_{in} by the OMIT process and the thermal component n_{th}. Note that, in our experiment, the probe field is a coherent state, which can be written as $c_{\text{in}} = \varepsilon_{\text{p}}$.

2. Dynamical evolution

In the phonon interference setup, the system timing shown in Fig. 5(a) is divided into four sections with different pulse durations, driving conditions, and the following initial conditions:

(1) First, without drive and probe fields ($c_{\text{in},0} = 0$, $G_0 = 0$), the mechanical mode undergoes a long free evolution period with a duration of t_1 to initialize n_{th} and let n_{coh} generated in the last experiment completely decays. In this section, it satisfies the initial conditions, $c_0(0) = c_0'(0) = 0$, $m_0(0) = \frac{2}{\gamma_{\text{m}}}B_{\text{in}}$, $m_0'(0) = (1 - B\frac{2}{\gamma_{\text{m}}})B_{\text{in}}$, which lead to a solution of

$$m_0(t) = \left[\left(\frac{2}{\gamma_{\text{m}}} - \frac{1}{B}\right)\exp\left(-Bt\right) + \frac{1}{B}\right]B_{\text{in}}, \tag{A17}$$

meaning a thermal noise power spectrum of thermal Brownian motion ($\frac{\gamma_{\text{m}} n_{\text{m}}}{\Delta^2 + \gamma_{\text{m}}^2/4}$) after enough evolution time ($Bt_1 \gg 1$) [20].

(2) Next, the system is driven by a pair of pulses consisting of a red detuning pump and a near-resonant probe, as shown in pulse 1 of Fig. 5(a). In this pulse pair, it satisfies the initial conditions, $c_1(0) = 0$, $c_1'(0) = A_{\text{in},1} - iGm_0(t_1)$, $m_1(0) = m_0(t_0)$, $m_1'(0) = B_{\text{in}} - Bm_0(t_1)$. Here, with $c_{\text{in},1} \neq 0$, $G_1 = g_{\text{o}}\sqrt{n_{\text{d},1}} \neq 0$, the dynamical evolution of $\langle m_1^\dagger m_1\rangle$ and $\langle c_1^\dagger c_1\rangle$ are shown in light pink shadow area of Figs. 5(b) and 5(c), respectively. It is noted that, in the simulation of Figs. 5(b) and 5(c), we select $\Delta = 0$. It can be seen that in Fig. 5(b), n_{coh} represented by the blue line gradually generates through the OMIT process. Meanwhile, n_{th} depicted by the red line decreases due to optomechanical backaction cooling [44]. Accordingly, in Fig. 5(c), the number of coherent photons in the optical cavity (blue line) gradually decreases due to its conversion to n_{coh} while the number of thermal photons in the optical cavity (red line) also decreases owe to the reduced n_{th}.

(3) Then, the system enters a period of free evolution ($c_{\text{in,f}} = 0$, $G_{\text{f}} = 0$) with a duration of T, after which n_{coh} generated in pulse 1 produces a phase φ_1. Additionally, n_{coh1} exponentially decays with a damping rate γ_{m} while n_{th} slightly increases due to the lack of optomechanical backaction cooling, as shown in the light blue shadow area of Fig. 5(b). However, as shown in the light blue shadow area of Fig. 5(c), $\langle c_{\text{f}}^\dagger c_{\text{f}}\rangle$ decays with a too large damping rate $\kappa_{\text{c}} \gg \gamma_{\text{m}}$ so that we can do an approximation of $\langle c_{\text{f}}^\dagger c_{\text{f}}\rangle \approx 0$ in this period.

(4) In the second pulse pairs, as shown in pulse 2 of Fig. 5(a), the system satisfies the initial conditions, $c_2(0) = 0$, $c_2'(0) = A_{\text{in2}} - iGm_{\text{f}}(T)$, $m_2(0) = m_{\text{f}}(T)$, $m_2'(0) = B_{\text{in}} - Bm_{\text{f}}(T)$, and driving conditions, $c_{\text{in},2} \approx c_{\text{in},1}$, $G_2 = g_{\text{o}}\sqrt{n_{\text{d},2}}$. These conditions result in a solution of

$$m = \sqrt{n_{\text{th}}}\frac{m_{\text{th}}}{|m_{\text{th}}|} + \sqrt{n_{\text{coh1}}}e^{i\varphi_1}\frac{c_{\text{in},1}}{|c_{\text{in},1}|} + \sqrt{n_{\text{coh2}}}e^{i\varphi_2}\frac{c_{\text{in},2}}{|c_{\text{in},2}|}. \tag{A18}$$

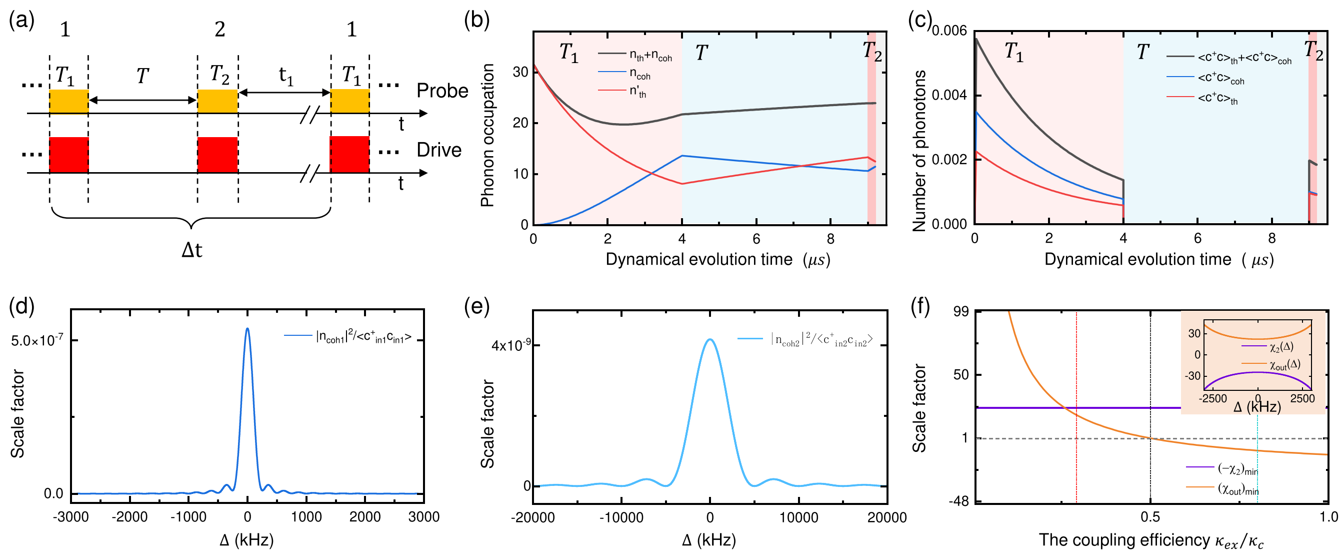

FIG. 5. (a) The sketch of one train of pulse pairs applied to optomechanical phonon interferometry. Δt represents the period of one experiment. T_1, T, and T_2, respectively indicate the duration of pulse 1, free evolution, and pulse 2. Before pulse 1, the system undergoes a long free evolution period to initialize the phonons. The pulses with different colors represent the probe field (yellow) and drive field (red), respectively. Panels (b) and (c) show the dynamical evolution of $\langle m^\dagger m(\Delta = 0)\rangle$ and $\langle c^\dagger c(\Delta = 0)\rangle$, respectively. The simulation parameter are $T_1 = 4$ μs, $T = 5$ μs, $T_2 = 0.2$ μs, $\kappa_c/2\pi = 880$ MHz, $\kappa_{ex}/\kappa_c = 0.27$, $\gamma_m/2\pi = 8$ kHz, $n_{d,1} = n_{d,3} = 22$, $g_o/2\pi = 800$ kHz, $\langle c^\dagger_{in,1}c_{in,1}\rangle = \langle c^\dagger_{in,2}c_{in,2}\rangle = 18$ μs^{-1}, and $n_{th} = 12.89$. Panels (d) and (e) show typical spectra of $n_{coh1}(\Delta)/\langle c^\dagger_{in,1}c_{in,1}\rangle$ and $n_{coh2}(\Delta)/\langle c^\dagger_{in,2}c_{in,2}\rangle$ at pulse 2. (f) The minimum values of scale factors of $-\chi_2(\Delta)$ and $\chi_{out}(\Delta)$ at pulse 2 ($t = T_2$) change via the coupling efficiency κ_{ex}/κ_c. The black dashed line ($\kappa_{ex}/\kappa_c = 0.5$) shows that $(\chi_{out})_{min} \approx 1$ while the orange dashed line ($\kappa_{ex}/\kappa_c = 0.27$) shows the coupling situation of OMCs device used in the experiment. The inset shows the spectra of scale factors of $\chi_2(\Delta)$ and $\chi_{out}(\Delta)$ at $\kappa_{ex}/\kappa_c = 0.27$.

Equation (A18) indicates that, in this case, besides the thermal component (n_{th}), the mechanical motion comprises a coherent component that includes the terms created by pulse 1 (n_{coh1}) and pulse 2 (n_{coh2}). The coherent component created by different pulses has different phases ($\varphi_1 \neq \varphi_2$) due to distinct processes of evolution. Specifically, n_{coh1} and n_{coh2} present a Lorentz-like distribution for different ω_p,

$$n_{coh1}(t) \approx \frac{\kappa_{ex} G^2 e^{-(\gamma_m + \frac{4G^2}{(\kappa_c-\gamma_m)})t - \gamma_m T}}{\left|\left(\frac{\kappa_c}{2}+i\Delta\right)\left(\frac{\gamma_m}{2}+i\Delta\right)+G^2\right|^2} \times \left|1 + e^{-(\frac{\gamma_m}{2}+\frac{2G^2}{(\kappa_c-\gamma_m)})T_1 - i\Delta T_1}\right|^2 \langle c^\dagger_{in,1}c_{in,1}\rangle, \quad \text{(A19)}$$

$$n_{coh2}(t) \approx \frac{\kappa_{ex} G^2 \left|1 + e^{-(\frac{\gamma_m}{2}+\frac{2G^2}{(\kappa_c-\gamma_m)})t - i\Delta t}\right|^2}{\left|\left(\frac{\kappa_c}{2}+i\Delta\right)\left(\frac{\gamma_m}{2}+i\Delta\right)+G^2\right|^2} \langle c^\dagger_{in,2}c_{in,2}\rangle, \quad \text{(A20)}$$

as shown in Figs. 5(d) and 5(e), respectively. In this approximation, $|x_{2,j}|T_j \gg 1$, j = 1, 2, f, so the terms with too quick decay rate ($x_{2,j}$) are neglected. The phases of coherent operators have

$$\varphi_1(t) \approx -\frac{\pi}{2} + \arg\left(1 + e^{-(\frac{\gamma_m}{2}+\frac{2G^2}{(\kappa_c-\gamma_m)})T_1 - i\Delta T_1}\right) + \Delta(T+t), \quad \text{(A21)}$$

$$\varphi_2(t) \approx -\frac{\pi}{2} + \arg\left(1 + e^{-(\frac{\gamma_m}{2}+\frac{2G^2}{(\kappa_c-\gamma_m)})t - i\Delta t}\right). \quad \text{(A22)}$$

For short enough t, $\varphi_2(t) \approx -\pi/2$, and $(\varphi_1 - \varphi_2)$ is approximately $\Delta T + \varphi_o$, where

$$\varphi_o(\Delta, T_1) \approx \arg\left(1 + e^{-(\frac{\gamma_m}{2}+\frac{2G^2}{(\kappa_c-\gamma_m)})T_1 - i\Delta T_1}\right)$$

can be approximated as a constant for a relatively long $\boldsymbol{T_1}$. Therefore, the phase difference $(\varphi_1 - \varphi_2)$ changes via different Δ and T. Meanwhile, the strength of amplitude of thermal operators can be written as

$$n_{th}(t) \approx \frac{n_m\left|\frac{\kappa_c}{2}(1 - B\nu_f(T))e^{-(\frac{\gamma_m}{2}+\frac{2G^2}{\kappa_a-\gamma_b})t - i\Delta t} + A\right|^2}{\left|\left(\frac{\kappa_c}{2}+i\Delta\right)\left(\frac{\gamma_m}{2}+i\Delta\right)+G^2\right|^2}, \quad \text{(A23)}$$

where $\nu_f(T) \approx [-1/B + \nu_1(T_1)]\exp(-BT) + 1/B$,

$$\nu_1(T_1) \approx \frac{\frac{\kappa_c}{2}[1 - B\nu_0(t_0)]e^{-(\frac{\gamma_m}{2}+\frac{2G^2}{\kappa_c-\gamma_m})T_1 - i\Delta T_1} + A}{\left(\frac{\kappa_c}{2}+i\Delta\right)\left(\frac{\gamma_m}{2}+i\Delta\right)+G^2},$$

and $\nu_0(t_1)$ [shown in Eq. (A17)] are respectively the final strength of amplitudes of thermal operators (m_{th}) for corresponding dynamical evolution sections (2), (1), (0).

Additionally, in this pulse, the analytical solution of the optical field in the cavity (c_2) can be expressed as

$$c_2(t) = -i\sqrt{P_s n_{th}}\frac{m_{th}}{|m_{th}|} - i\sqrt{P_s n_{coh1}}e^{i\varphi_1}\frac{c_{in,1}}{|c_{in,1}|} - \left(i\sqrt{P_s n_{coh2}}e^{i\varphi_2} - iC_p e^{i\varphi_{2,o}}\right)\frac{c_{in,2}}{|c_{in,2}|}, \quad \text{(A24)}$$

which represents that the part of intracavity optical fields originated from the optomechanical scattering of phonons by a scattering probability $P_s \approx |2G/(\kappa_c - \gamma_m)|^2$. Here, the strength of

$$C_p \approx \left|\frac{\sqrt{\kappa_{ex}\langle c^\dagger_{in,2}c_{in,2}\rangle}}{\kappa_c/2 + i\Delta}\right|,$$

and $\varphi_{2,\mathrm{o}} \approx \varphi_2 \approx -\pi/2$. The term $-iC_\mathrm{p}e^{i\varphi_{2,\mathrm{o}}}$ represents the residual probe field which does not participate in the optomechanical interaction. After defining a scale factor $-\chi_2 \approx C_\mathrm{p}/\sqrt{P_\mathrm{s}n_{\mathrm{coh}2}} - 1 \geqslant 1$, which is described by the purple line in Fig. 5(f), the c_2 can be simplified as

$$c_2(t) = -i\sqrt{P_\mathrm{s}n_\mathrm{th}}\frac{m_\mathrm{th}}{|m_\mathrm{th}|} - i\sqrt{P_\mathrm{s}n_{\mathrm{coh}1}}e^{i\varphi_1}\frac{c_{\mathrm{in},1}}{|c_{\mathrm{in},1}|} - i\sqrt{P_\mathrm{s}n_{\mathrm{coh}2}}\chi_2 e^{i\varphi_2}\frac{c_{\mathrm{in},2}}{|c_{\mathrm{in},2}|}. \tag{A25}$$

Therefore, during pulse 2, the dynamical evolution of $\langle m_2^\dagger m_2\rangle$ and $\langle c_2^\dagger c_2\rangle$ can be derived:

$$\langle m_2^\dagger m_2\rangle = n_\mathrm{th} + n_{\mathrm{coh}1} + n_{\mathrm{coh}2} + 2\sqrt{n_{\mathrm{coh}1}n_{\mathrm{coh}2}}\cos(\varphi_1 - \varphi_2), \tag{A26}$$

$$\langle c_2^\dagger c_2\rangle \approx P_\mathrm{s}\big[n_\mathrm{th} + n_{\mathrm{coh}1} + |\chi_2|^2 n_{\mathrm{coh}2} + 2\mathrm{Re}\big(\chi_2\sqrt{n_{\mathrm{coh}1}n_{\mathrm{coh}2}}e^{i(\varphi_1-\varphi_2)}\big)\big], \tag{A27}$$

which are respectively shown in the dark pink shadow area of Figs. 5(b) and 5(c). Note that, in the simulation of Figs. 5(b) and 5(c), we simply consider the thermal component n_th of mechanical motion using an integral mean thermal phonon occupation, i.e., $\int_{\omega_\mathrm{p}} n_\mathrm{th} d\omega_\mathrm{p}$. Our detection system cannot distinguish n_th with different frequencies, in other words, n_th of all frequency, need to be considered when we calibrate the phonon population at any ω_p. For the sake of simplicity, we still depict this integral mean thermal phonon occupation as n_th in the following description.

3. Phonon interference on photon count rate

As mentioned earlier, the phase difference of $(\varphi_1 - \varphi_2) \approx \Delta T + \varphi_\mathrm{o}$ varies periodically from 0 to 2π as Δ or T changes, which leads to an interference fringe of the (coherent) phonon population via Δ or T, i.e., the phonon interference. To measure these interference fringes of $\langle m_2^\dagger m_2\rangle$, the output optical signal field (c_out) is considered. According to the input-output theory, $c_\mathrm{out} = c_\mathrm{in} - \sqrt{\kappa_\mathrm{ex}}c$, the output signal field in pulse 2 can be generally written as

$$c_\mathrm{out} = i\sqrt{\kappa_\mathrm{ex}P_\mathrm{s}n_\mathrm{th}}\frac{m_\mathrm{th}}{|m_\mathrm{th}|} + i\sqrt{\kappa_\mathrm{ex}P_\mathrm{s}n_{\mathrm{coh}1}}e^{i\varphi_1}\frac{c_{\mathrm{in},1}}{|c_{\mathrm{in},1}|} + (1 - i\sqrt{\kappa_\mathrm{ex}}C_\mathrm{p}e^{i\varphi_{2,\mathrm{o}}} + i\sqrt{\kappa_\mathrm{ex}P_\mathrm{s}n_{\mathrm{coh}2}}e^{i\varphi_2})\frac{c_{\mathrm{in},2}}{|c_{\mathrm{in},2}|}. \tag{A28}$$

It is worth noting that when the OMCs device is near critical coupling, $i\sqrt{\kappa_\mathrm{ex}}C_\mathrm{p}e^{i\varphi_{2,\mathrm{o}}} \approx 1$,

$$c_\mathrm{out} \approx i\sqrt{\kappa_\mathrm{ex}P_\mathrm{s}}m_2, \tag{A29}$$

which indicates that c_out has the same characteristics as m_2. When an OMC device is over- or undercoupled, we define

$$\chi_\mathrm{out} \approx 1 - \frac{C_\mathrm{p}}{\sqrt{P_\mathrm{s}n_{\mathrm{coh}2}}} + \frac{1}{\sqrt{\kappa_\mathrm{ex}P_\mathrm{s}n_{\mathrm{coh}2}}},$$

which is described by the orange line in Fig. 5(f), then

$$c_\mathrm{out} \approx i\sqrt{\kappa_\mathrm{ex}P_\mathrm{s}n_\mathrm{th}}\frac{m_\mathrm{th}}{|m_\mathrm{th}|} + i\sqrt{\kappa_\mathrm{ex}P_\mathrm{s}n_{\mathrm{coh}1}}e^{i\varphi_1}\frac{c_{\mathrm{in},1}}{|c_{\mathrm{in},1}|} - i\sqrt{\kappa_\mathrm{ex}P_\mathrm{s}n_{\mathrm{coh}2}}\chi_\mathrm{out}e^{i\varphi_2}\frac{c_{\mathrm{in},2}}{|c_{\mathrm{in},2}|}, \tag{A30}$$

and the number of output signal photons can be derived,

$$\langle c_\mathrm{out}^\dagger c_\mathrm{out}\rangle \approx \kappa_\mathrm{ex}P_\mathrm{s}\big[n_\mathrm{th} + n_{\mathrm{coh}1} + |\chi_\mathrm{out}|^2 n_{\mathrm{coh}2} + 2\mathrm{Re}\big(\chi_\mathrm{out}\sqrt{n_{\mathrm{coh}1}n_{\mathrm{coh}2}}e^{i(\varphi_1-\varphi_2)}\big)\big], \tag{A31}$$

where the visibility of the interference of $\langle c_\mathrm{out}^\dagger c_\mathrm{out}\rangle$ is amplified by a factor

$$\chi_\mathrm{out} \approx 1 - \frac{C_\mathrm{p}}{\sqrt{P_\mathrm{s}n_{\mathrm{coh}2}}} + \frac{1}{\sqrt{\kappa_\mathrm{ex}P_\mathrm{s}n_{\mathrm{coh}2}}}$$

from the visibility of the interference of $\langle m_2^\dagger m_2\rangle$. Meanwhile, when the OMC device is undercoupled (overcoupled), the interference fringes of $\langle c_\mathrm{out}^\dagger c_\mathrm{out}\rangle$ is consistent (contrary) with the interference of $\langle m_2^\dagger m_2\rangle$, as shown in the pink (green) line of Fig. 6.

The simulation of a 2D phonon interference fringes of $\langle c_\mathrm{out}^\dagger c_\mathrm{out}\rangle$ via Δ and T with $n_\mathrm{th}(t = T_1 + 5\mu\mathrm{s}) = 12.89$, $n_\mathrm{coh}/n_\mathrm{th}(t = T_1 + 5\,\mu\mathrm{s}, \Delta = 0) = 3.26$ ($\langle c_{\mathrm{in},1}^\dagger c_{\mathrm{in},1}\rangle = \langle c_{\mathrm{in},2}^\dagger c_{\mathrm{in},2}\rangle = 93\ \mu\mathrm{s}^{-1}$), $\kappa_\mathrm{c}/2\pi = 880$ MHz, $\kappa_\mathrm{ex}/\kappa_\mathrm{c} = 0.27$, $\gamma_\mathrm{m}/2\pi = 8$ kHz, $n_{\mathrm{d},1} = n_{\mathrm{d},2} = 22$, $g_\mathrm{o}/2\pi = 800$ kHz, $T_1 = 4\ \mu\mathrm{s}$, $T_2 = 0.4\ \mu\mathrm{s}$ are calculated and shown in Fig. 3(a) of the main text. The distinct spectral oscillations observed in Fig. 3(a) demonstrate the phonon fringes. The increase in time T leads to a decreased period of the phonon fringe, which is expected by the previous theoretical derivation, i.e., $(\varphi_1 - \varphi_2) \approx \Delta T + \varphi_\mathrm{o}$.

We can derive the interference visibility on normalized photon count rates, as it satisfies the conditions: $\kappa_\mathrm{c} \gg \gamma_\mathrm{m}, \Delta$,

$$V_\mathrm{count} = (I_\mathrm{max} - I_\mathrm{min})/(I_\mathrm{max} + I_\mathrm{min}) = \frac{n_{\mathrm{coh},\Delta=0,t=T_1+T}/n_\mathrm{th}(\zeta_{\Delta_1} - \zeta_{\Delta_2})}{2 + n_{\mathrm{coh},\Delta=0,t=T_1+T}/n_\mathrm{th}(\zeta_{\Delta_1} + \zeta_{\Delta_2})}, \tag{A32}$$

where $n_{\mathrm{coh},\Delta=0,t=T_1+T}/n_\mathrm{th}$ can be experimental calibration (as described in Sec. II), $\eta = \kappa_\mathrm{ex}/\kappa_\mathrm{c}$, $C = 4G^2/\kappa_\mathrm{c}\gamma_\mathrm{m}$, and

$$\zeta_\Delta(\gamma_\mathrm{m}, C, t, T, T_1, \langle c_{\mathrm{in},1}^\dagger c_{\mathrm{in},1}\rangle, \langle c_{\mathrm{in},2}^\dagger c_{\mathrm{in},2}\rangle) = \frac{n_{\mathrm{coh}1} + |\chi_\mathrm{out}|^2 n_{\mathrm{coh}2} + 2\mathrm{Re}\big(\chi_\mathrm{out}\sqrt{n_{\mathrm{coh}1}n_{\mathrm{coh}2}}e^{i(\varphi_1-\varphi_2)}\big)}{n_{\mathrm{coh},\Delta=0,t=T_1+T}} \approx \frac{(1+C)^2}{e^{-\gamma_\mathrm{m}(1+C)T_1-\gamma_\mathrm{m}CT}(1+e^{-\frac{\gamma_\mathrm{m}}{2}(1+C)T_1})^2}\left\{\frac{e^{-\gamma_\mathrm{m}(1+C)t-\gamma_\mathrm{m}T}\left|1+e^{-\frac{\gamma_\mathrm{m}}{2}(1+C)T_1-i\Delta T_1}\right|^2}{\left|1+C+i\frac{2\Delta}{\gamma_\mathrm{m}}\right|^2}\right.$$

$$+\left[1-\frac{\left|1+C+i\frac{2\Delta}{\gamma_m}\right|}{C\left|1+e^{-\frac{\gamma_m}{2}(1+C)t-i\Delta t}\right|}\left(1-\frac{1}{2\eta\sqrt{\langle c_{\mathrm{in},2}^{\dagger}c_{\mathrm{in},2}\rangle}}\right)\right]^2\frac{\left|1+e^{-\frac{\gamma_m}{2}(1+C)t-i\Delta t}\right|^2}{\left|1+C+i\frac{2\Delta}{\gamma_m}\right|^2}\frac{\langle c_{\mathrm{in},2}^{\dagger}c_{\mathrm{in},2}\rangle}{\langle c_{\mathrm{in},1}^{\dagger}c_{\mathrm{in},1}\rangle}$$

$$+2\left[1-\frac{\left|1+C+i\frac{2\Delta}{\gamma_m}\right|}{C\left|1+e^{-\frac{\gamma_m}{2}(1+C)t-i\Delta t}\right|}\left(1-\frac{1}{2\eta\sqrt{\langle c_{\mathrm{in},2}^{\dagger}c_{\mathrm{in},2}\rangle}}\right)\right]\frac{\left|1+e^{-\frac{\gamma_m}{2}(1+C)T_1-i\Delta T_1}\right|}{\left|1+C+i\frac{2\Delta}{\gamma_m}\right|^2}$$

$$\left.\times\left|1+e^{-\frac{\gamma_m}{2}(1+C)t-i\Delta t}\right|e^{-\frac{\gamma_m(1+C)t+\gamma_m T}{2}}\sqrt{\frac{\langle c_{\mathrm{in},2}^{\dagger}c_{\mathrm{in},2}\rangle}{\langle c_{\mathrm{in},1}^{\dagger}c_{\mathrm{in},1}\rangle}}\cos(\Delta T+\varphi_o)\right\}. \tag{A33}$$

As shown in Eq. (A29), for given γ_m, C, t, T, T_1, $\langle c_{\mathrm{in},1}^{\dagger}c_{\mathrm{in},1}\rangle$, $\langle c_{\mathrm{in},2}^{\dagger}c_{\mathrm{in},2}\rangle$, ζ_Δ is just a function of Δ, and we denote ζ_{Δ_1} (ζ_{Δ_2}) as the maximum (minimum) value for all of Δ. Therefore, we can extract the interference visibility V_{count} by Eq. (A28). Furthermore, in our experiment, we have also studied the interference visibility with the same approach for another γ_m, C. In fact, for a determined device, κ_c and g_o are constants, thus we can denote that $C=\frac{4g_o^2 n_d}{\kappa_c\gamma_m}=C(\gamma_m,n_d)$. In total, in this paper, we can describe the interference visibility on normalized photon count rates as Eq. (A28) in which $V_{\mathrm{count}}=V_{\mathrm{count}}(n_{\mathrm{coh},\Delta=0,t=T_1+T}/n_{\mathrm{th}},\gamma_m,C)=V_{\mathrm{count}}(n_{\mathrm{coh},\Delta=0,t=T_1+T}/n_{\mathrm{th}},\gamma_m,n_d)$ for a given t, T, T_1, $\langle c_{\mathrm{in},1}^{\dagger}c_{\mathrm{in},1}\rangle$, $\langle c_{\mathrm{in},2}^{\dagger}c_{\mathrm{in},2}\rangle$.

4. Phonon interference on the second-order correlation function

Different from classical optomechanical phonon interferometry [16], where n_{coh} is so large that n_{th} is generally negligible, in this single-phonon-level optomechanical phonon interferometry, n_{coh} and n_{th} are closer. Therefore, for different Δ or T, the interference fringes of n_{coh} can result in considerable interference fringes in the ratio of $n_{\mathrm{th}}/n_{\mathrm{coh}}$. However, due to the different quantum statistical properties of n_{coh} and n_{th}, the interference fringes in the ratio value of $n_{\mathrm{th}}/n_{\mathrm{coh}}$ lead to density correlation interference fringes. The density correlation of phonons can be indicated by the second-order correlation functions

$$g^{(2)}(\tau)=\frac{\langle m^{\dagger}(0)m^{\dagger}(\tau)m(\tau)m(0)\rangle}{\langle m^{\dagger}(0)m(0)\rangle}.$$

While the phonons generated from different ($\tau\neq 0$) pulse sequences are uncorrelated, $g^{(2)}(\tau)=1$. Therefore, only $g^{(2)}(0)$ is considered. There are the four order relationships:

$$\langle c_{\mathrm{in}}^{\dagger}c_{\mathrm{in}}c_{\mathrm{in}}^{\dagger}c_{\mathrm{in}}\rangle=\langle c_{\mathrm{in}}^{\dagger}c_{\mathrm{in}}\rangle^2+\langle c_{\mathrm{in}}^{\dagger}c_{\mathrm{in}}\rangle, \tag{A34}$$

$$\langle m_{\mathrm{th}}^{\dagger}m_{\mathrm{th}}m_{\mathrm{th}}^{\dagger}m_{\mathrm{th}}\rangle=2n_m^2+n_m. \tag{A35}$$

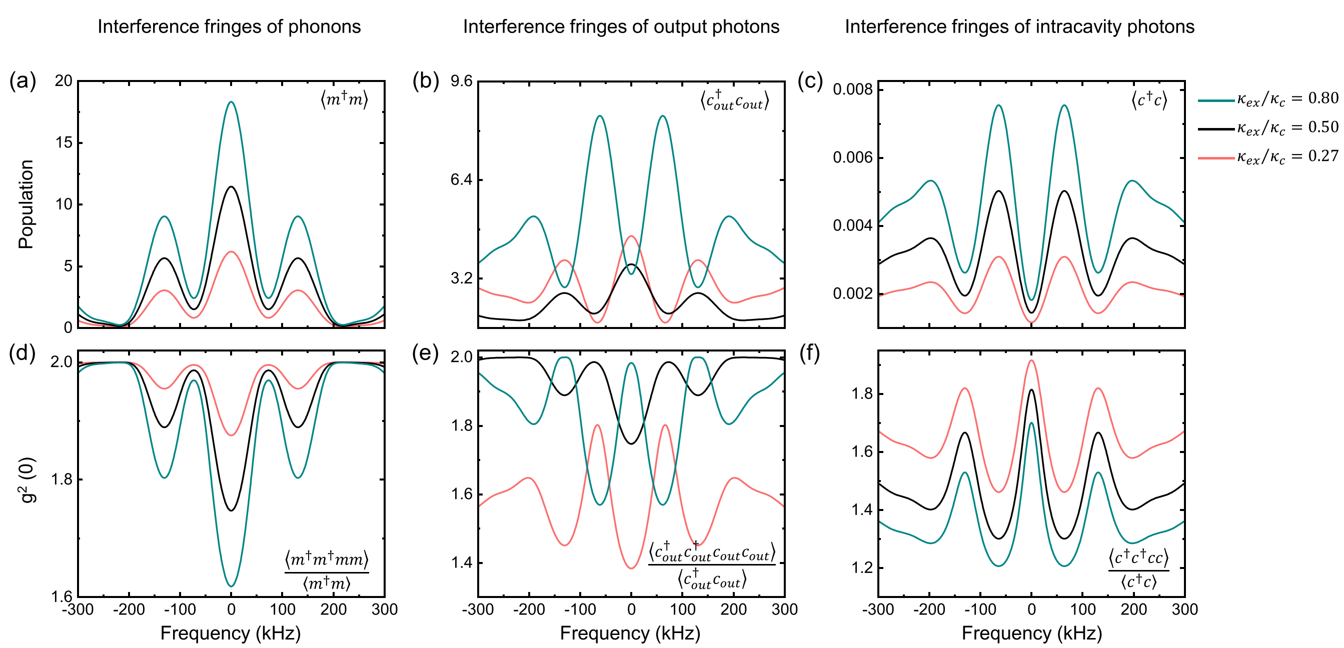

FIG. 6. Phonon interference fringes with simulation parameter: $\kappa_{\mathrm{ex}}/\kappa_c=0.27$, 0.50, 0.80 (respectively shown by the pink, black, and green line), and $\kappa_c/2\pi=880$ MHz, $\gamma_m/2\pi=8$ kHz, $n_{d,1}=n_{d,2}=22$, $g_o/2\pi=800$ kHz, $T_1=4$ μs, $T=5$ μs, $T_2=0.8$ μs, $n_{\mathrm{th}}=12.89$, $\langle c_{\mathrm{in},1}^{\dagger}c_{\mathrm{in},1}\rangle=\langle c_{\mathrm{in},2}^{\dagger}c_{\mathrm{in},2}\rangle=8$ μs^{-1}. The upper panel is the RI fringes in the population for (a) phonons, (b) output signal photons, and (c) intracavity photons. The bottom panel is the corresponding RI fringes on second-order correlation functions $g^{(2)}(0)$.

Therefore, substituting Eq. (A18), $g^{(2)}(0)$ can be calculated:

$$g^{(2)}(0) = 1 + \frac{n_{\rm th}^2 + 2(n_{\rm coh1} + n_{\rm coh2})n_{\rm th}}{\langle m_2^\dagger m_2\rangle^2} + \frac{4\sqrt{n_{\rm coh1}n_{\rm coh2}}\cos(\varphi_1 - \varphi_2)n_{\rm th}}{\langle m_2^\dagger m_2\rangle^2}, \tag{A36}$$

which can be simplified to

$$g^{(2)}(0) = 1 + \frac{n_{\rm th}^2 + 2n_{\rm coh}n_{\rm th}}{(n_{\rm th} + n_{\rm coh})^2} = 2 - \frac{1}{\left(1 + \frac{n_{\rm th}}{n_{\rm coh}}\right)^2}, \tag{A37}$$

where $n_{\rm coh} = n_{\rm coh1} + n_{\rm coh2} + 2\sqrt{n_{\rm coh1}\,n_{\rm coh2}}\cos(\varphi_1 - \varphi_2)$. Equation (A37) shows that the interference fringes of the second-order correlation functions $g^{(2)}(0)$ are negatively correlated with the interference fringes of $n_{\rm coh}$ (or $\langle m_3^\dagger m_3\rangle$), which can be observed respectively in the bottom panel and upper panel of Fig. 6. Using Eq. (A30), this interference fringes in the density correlation of the phonons can be mapped to the counterpart of output signal photons. The corresponding simulation of 2D phonon interference fringes of $g^{(2)}(0)$ of output signal photons is calculated and shown in Fig. 3(b) of the main text, which has a contrary interference fringe with Fig. 3(a). Note that this derivation of $g^{(2)}(0)$, which contains both the coherent and thermal components, is in good agreement with the corresponding results in Ref. [45].

Similarly, we can derive the interference visibility on $g^{(2)}(0)$ when it satisfies the conditions $\kappa_{\rm c} \gg \gamma_{\rm m}, \Delta$:

$$\begin{aligned} V_{g^{(2)}(0)} &= \frac{[g^{(2)}(0)]_{\max} - [g^{(2)}(0)]_{\min}}{[g^{(2)}(0)]_{\max} + [g^{(2)}(0)]_{\min}} \\ &= \left[\frac{1}{\left(1 + \frac{n_{\rm th}\zeta_{\Delta_1}^{-1}}{n_{{\rm coh},\Delta=0,t=T_1+T}}\right)^2} - \frac{1}{\left(1 + \frac{n_{\rm th}\zeta_{\Delta_2}^{-1}}{n_{{\rm coh},\Delta=0,t=T_1+T}}\right)^2}\right] \\ &\quad \times \left\{4 - \frac{1}{\left(1 + \frac{n_{\rm th}\zeta_{\Delta_1}^{-1}}{n_{{\rm coh},\Delta=0,t=T_1+T}}\right)^2} - \frac{1}{\left(1 + \frac{n_{\rm th}\zeta_{\Delta_2}^{-1}}{n_{{\rm coh},\Delta=0,t=T_1+T}}\right)^2}\right\}^{-1}. \end{aligned} \tag{A38}$$

Through Eq. (A34), we similarly have

$$V_{g^{(2)}(0)} = V_{g^{(2)}(0)}\left(\frac{n_{{\rm coh},\Delta=0,t=T_1+T}}{n_{\rm th}}, \gamma_{\rm m}, n_{\rm d}\right)$$

for a given t, T, T_1, $\langle c_{{\rm in},1}^\dagger c_{{\rm in},1}\rangle$, and $\langle c_{{\rm in},2}^\dagger c_{{\rm in},2}\rangle$.

In conclusion, we can simultaneously obtain the information of both $n_{\rm th} + n_{\rm coh}$ and $n_{\rm th}/n_{\rm coh}$ by the intensity and correlation measurements. Especially for the quantum states, where $g^{(2)} \gg 1$ or $\ll 1$, the second-order correlation value of the Ramsey interference will oscillate wildly from the minimum to maximum, which will bring huge advantages in the field of quantum precision sensing.

APPENDIX B: EXPERIMENTAL RESULTS

1. Fabrication

The devices were patterned by *e*-beam lithography (EBL) with ARP6200 09 resist on a silicon-on-insulator (SOI) wafer from SOITEC (resistivity 10–20 Ω cm, device layer thickness 220 nm, buried-oxide layer thickness 2 μm). Following the development of the pattern, the film was etched with a C_4F_8/SF_6-based gas in an inductively coupled plasma (ICP) etcher. The Si device layer was then masked using AZ4620 photoresist to define a mesa region of the chip to which a tapered lensed fiber can access. Outside of the protected mesa region, the buried oxide was removed with a plasma etch and a trench is formed in the underlying silicon substrate using a deep silicon etching process. The devices were then released in vapor hydrofluoric using HF-Etching-SPTS-uEtch and cleaned in a piranha solution (3 : 1 H_2SO_4 : H_2O_2) before a final hydrogen termination in diluted HF (1% aqueous HF solution).

2. Calibration of mean thermal photon occupations and coherent phonon occupations

To experimentally determine the mean thermal phonon occupation $n_{\rm th}(t = T_1 + T)$ and coherent phonon occupations $n_{\rm coh}(\Delta = 0, t = T_1 + T)$ for the optomechanical phonon interferometry, we performed a series of calibration measurements with different driving regimes. First, we sent trains of alternating blue- or red-detuned optical pulses ($\approx\omega_{\rm c} \pm \omega_{\rm m}$) with a duration of 40 ns to the OMC device, as shown in the

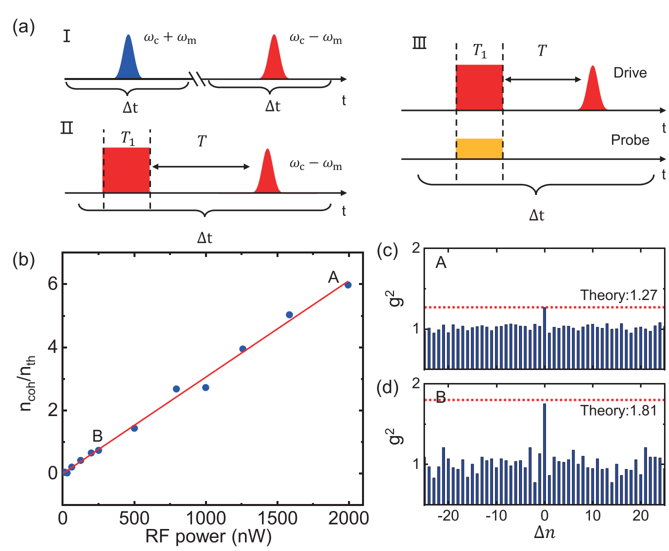

FIG. 7. Calibration of the mean thermal phonon occupations and coherent phonon occupations. (a) Sketch of one train of pulse pairs applied to calibrate (I) $n_{\rm th,0}$ that thermalizes at cryogenic temperatures, (II) $n_{\rm th}(t = T_1 + T)$ after implementing an additional red-detuning driving pulse, (III) $n_{\rm coh}(\Delta = 0, t = T_1 + T)$. (b) The ratio $n_{\rm coh}(\Delta = 0, t = T_1 + T)/n_{\rm th}(t = T_1 + T)$ via the weak rf input power of the EOM with $n_{\rm th}(T_1 + T) = 12.89$, where $T_1 = 4$ μs and $T = 5$ μs. Panels (c) and (d) respectively show the corresponding $g^{(2)}(\tau)$ of the points A and B in panel (b). The red lines indicate the theory value of $g^{(2)}(0)$ from Eq. (A6) using the calibrated ratio $n_{\rm coh}/n_{\rm th}$ from panel (b).

upper panel I of Fig. 7(a). From the asymmetry in count rates of these two processes, we can calculate the $n_{\text{th},0}$ that thermalizes at cryogenic temperatures [46]. The results are shown in Fig. 2(d), corresponding to a mean thermal occupation of $n_{\text{th},0} = 0.071 \pm 0.008$. Note that the tunable laser is a Toptica CTL 1550, and the filter used here is a Micron Optics, FFT-TF2. In the bottom panel II of Fig. 7(a), after implementing an additional red-detuning ($\omega_c - \omega_m$) driving pulse (with a duration of T_1) to mimic the same heating conditions as in the experiment, we further calibrate $n_{\text{th}}(t = T_1 + T)$ using phonon counting technology [42]. Specifically, in one train, a second red-detuning optical pulse with a duration of 40 ns, which is T behind the additional driving pulse, is next sent to the device. In this case, the count rate of the anti-Stokes process in the second pulse is proportional to $n_{\text{th}}(t = T_1 + T)$ with a scaling factor of $\Gamma_{\text{antiStokes}}$. While the peak power and duration of the second pulse in the bottom panel II of Fig. 7(a) are the same as those in the upper panel I of Fig. 7(a), the scaling factor $\Gamma_{\text{antiStokes}}$ is also the same [42]. Therefore, by using $\Gamma_{\text{antiStokes}}$ derived from $n_{\text{th},0}$, $n_{\text{th}}(T_1 + T) = 12.89$ is calibrated, where $T_1 = 4$ μs and $T = 5$ μs.

Finally, the calibration of $n_{\text{coh}}(\Delta = 0, t = T_1 + T)$ for the optomechanical phonon interferometry is conducted. As shown in the right panel III of Fig. 7(a), for the preparation of coherent phonons, an additional probe pulse ($\Delta = 0$) with the same duration of T_1 is sent to the device. The probe pulses are blue-detuned with drive pulses modulated by the EOM. Through OMIT technology, the tunable $n_{\text{coh}}(\Delta = 0, t = T_1 + T)$ can be nearly linearly controlled by changing the weak rf input power of the EOM. To calibrate the total phonon occupation (including n_{th} and n_{coh}), similarly, in one train, a second red-detuning optical pulse (40 ns, T behind the first pulse) is sent to the device. $n_{\text{coh}}(\Delta = 0, t = T_1 + T)$ is calculated by subtracting n_{th} from the total phonon occupation, where the heating effect of a very weak probe is neglected. As a result, the count rate of the anti-Stokes process at the second pulse is proportional to the weak rf input power of the EOM, as shown in Fig. 7(b). To further determine $n_{\text{coh}}(\Delta = 0, t = T_1 + T)$, the second-order correlation function $g^{(2)}(\tau)$ of the scattered photons from the second red-detuning optical pulse is experimentally performed to determine the ratio $n_{\text{coh}}(\Delta = 0, t = T_1 + T)/n_{\text{th}}(t = T_1 + T)$. The corresponding $g^{(2)}(\tau)$ of points A and B in Fig. 7(b) are shown in Figs. 7(c) and 7(d), respectively. The red lines indicate the theory value of $g^{(2)}(0)$ from Eq. (A6) using the ratios $n_{\text{coh}}/n_{\text{th}}$ calibrated as described above. The theory value of $g^{(2)}(0)$ and experimental $g^{(2)}(0)$ are entirely consistent. Note that the measurement of $g^{(2)}$ needs a sufficient number of events, otherwise, it will lead to fluctuations similar to Fig. 7(d).

[1] N. F. Ramsey, A molecular beam resonance method with separated oscillating fields, Phys. Rev. **78**, 695 (1950).

[2] M. Salour, Quantum interference effects in two-photon spectroscopy, Rev. Mod. Phys. **50**, 667 (1978).

[3] J. E. Thomas, P. R. Hemmer, S. Ezekiel, C. C. Leiby, Jr., R. H. Picard, and C. R. Willis, Observation of Ramsey fringes using a stimulated, resonance raman transition in a sodium atomic beam, Phys. Rev. Lett. **48**, 867 (1982).

[4] G. Santarelli, P. Laurent, P. Lemonde, A. Clairon, A. G. Mann, S. Chang, A. N. Luiten, and C. Salomon, Quantum projection noise in an atomic fountain: A high stability cesium frequency standard, Phys. Rev. Lett. **82**, 4619 (1999).

[5] T. Zanon, S. Guérandel, E. de Clercq, D. Holleville, N. Dimarcq, and A. Clairon, High contrast Ramsey fringes with coherent-population-trapping pulses in a double lambda atomic system, Phys. Rev. Lett. **94**, 193002 (2005).

[6] M. Schioppo, R. C. Brown, W. F. McGrew, N. Hinkley, R. J. Fasano, K. Beloy, T. Yoon, G. Milani, D. Nicolodi, J. Sherman *et al.*, Ultrastable optical clock with two cold-atom ensembles, Nat. Photon. **11**, 48 (2017).

[7] E. A. Donley, N. R. Claussen, S. T. Thompson, and C. E. Wieman, Atom–molecule coherence in a Bose–Einstein condensate, Nature (London) **417**, 529 (2002).

[8] X. Maître, E. Hagley, G. Nogues, C. Wunderlich, P. Goy, M. Brune, J. M. Raimond, and S. Haroche, Quantum memory with a single photon in a cavity, Phys. Rev. Lett. **79**, 769 (1997).

[9] S. Deleglise, I. Dotsenko, C. Sayrin, J. Bernu, M. Brune, J.-M. Raimond, and S. Haroche, Reconstruction of non-classical cavity field states with snapshots of their decoherence, Nature (London) **455**, 510 (2008).

[10] P. Schindler, M. Müller, D. Nigg, J. T. Barreiro, E. A. Martinez, M. Hennrich, T. Monz, S. Diehl, P. Zoller, and R. Blatt, Quantum simulation of dynamical maps with trapped ions, Nat. Phys. **9**, 361 (2013).

[11] S. Clemmen, A. Farsi, S. Ramelow, and A. L. Gaeta, Ramsey interference with single photons, Phys. Rev. Lett. **117**, 223601 (2016).

[12] B. Pingault, D.-D. Jarausch, C. Hepp, L. Klintberg, J. N. Becker, M. Markham, C. Becher, and M. Atatüre, Coherent control of the silicon-vacancy spin in diamond, Nat. Commun. **8**, 15579 (2017).

[13] S. Cavalieri, R. Eramo, M. Materazzi, C. Corsi, and M. Bellini, Ramsey-type spectroscopy with high-order harmonics, Phys. Rev. Lett. **89**, 133002 (2002).

[14] D. Leibfried, M. D. Barrett, T. Schaetz, J. Britton, J. Chiaverini, W. M. Itano, J. D. Jost, C. Langer, and D. J. Wineland, Toward Heisenberg-limited spectroscopy with multiparticle entangled states, Science **304**, 1476 (2004).

[15] T. Faust, J. Rieger, M. J. Seitner, J. P. Kotthaus, and E. M. Weig, Coherent control of a classical nanomechanical two-level system, Nat. Phys. **9**, 485 (2013).

[16] K. Qu, C. Dong, H. Wang, and G. S. Agarwal, Optomechanical Ramsey interferometry, Phys. Rev. A **90**, 053809 (2014).

[17] A. Asadian, C. Brukner, and P. Rabl, Probing macroscopic realism via Ramsey correlation measurements, Phys. Rev. Lett. **112**, 190402 (2014).

[18] T. Delord, P. Huillery, L. Schwab, L. Nicolas, L. Lecordier, and G. Hétet, Ramsey interferences and spin echoes from electron spins inside a levitating macroscopic particle, Phys. Rev. Lett. **121**, 053602 (2018).

[19] M. Aspelmeyer, P. Meystre, and K. Schwab, Quantum optomechanics, Phys. Today **65**(7), 29 (2012).
[20] M. Aspelmeyer, T. J. Kippenberg, and F. Marquardt, Cavity optomechanics, Rev. Mod. Phys. **86**, 1391 (2014).
[21] D. J. Wilson, V. Sudhir, N. Piro, R. Schilling, A. Ghadimi, and T. J. Kippenberg, Measurement-based control of a mechanical oscillator at its thermal decoherence rate, Nature (London) **524**, 325 (2015).
[22] S.-J. Tang, M. Zhang, J. Sun, J.-W. Meng, X. Xiong, Q. Gong, D. Jin, Q.-F. Yang, and Y.-F. Xiao, Single-particle photoacoustic vibrational spectroscopy using optical microresonators, Nat. Photon. **17**, 951 (2023).
[23] J. Guo and S. Gröblacher, Integrated optical-readout of a high-Q mechanical out-of-plane mode, Light: Sci. Appl. **11**, 282 (2022).
[24] C. Dong, V. Fiore, M. C. Kuzyk, and H. Wang, Optomechanical dark mode, Science **338**, 1609 (2012).
[25] Z. Shen, Y.-L. Zhang, Y. Chen, Y.-F. Xiao, C.-L. Zou, G.-C. Guo, and C.-H. Dong, Nonreciprocal frequency conversion and mode routing in a microresonator, Phys. Rev. Lett. **130**, 013601 (2023).
[26] A. Youssefi, S. Kono, A. Bancora, M. Chegnizadeh, J. Pan, T. Vovk, and T. J. Kippenberg, Topological lattices realized in superconducting circuit optomechanics, Nature (London) **612**, 666 (2022).
[27] R. Riedinger, A. Wallucks, I. Marinković, C. Löschnauer, M. Aspelmeyer, S. Hong, and S. Gröblacher, Remote quantum entanglement between two micromechanical oscillators, Nature (London) **556**, 473 (2018).
[28] S. Barzanjeh, E. Redchenko, M. Peruzzo, M. Wulf, D. Lewis, G. Arnold, and J. M. Fink, Stationary entangled radiation from micromechanical motion, Nature (London) **570**, 480 (2019).
[29] P. Arrangoiz-Arriola, E. A. Wollack, Z. Wang, M. Pechal, W. Jiang, T. P. McKenna, J. D. Witmer, R. Van Laer, and A. H. Safavi-Naeini, Resolving the energy levels of a nanomechanical oscillator, Nature (London) **571**, 537 (2019).
[30] G. S. MacCabe, H. Ren, J. Luo, J. D. Cohen, H. Zhou, A. Sipahigil, M. Mirhosseini, and O. Painter, Nano-acoustic resonator with ultralong phonon lifetime, Science **370**, 840 (2020).
[31] M. Mirhosseini, A. Sipahigil, M. Kalaee, and O. Painter, Superconducting qubit to optical photon transduction, Nature (London) **588**, 599 (2020).
[32] R. Hanbury Brown and R. Q. Twiss, A test of a new type of stellar interferometer on Sirius, Nature (London) **178**, 1046 (1956).
[33] A. Abeysekara, W. Benbow, A. Brill, J. Buckley, J. Christiansen, A. Chromey, M. Daniel, J. Davis, A. Falcone, Q. Feng *et al.*, Demonstration of stellar intensity interferometry with the four VERITAS telescopes, Nat. Astron. **4**, 1164 (2020).
[34] R. J. Glauber, The quantum theory of optical coherence, Phys. Rev. **130**, 2529 (1963).
[35] H. J. Kimble, M. Dagenais, and L. Mandel, Photon antibunching in resonance fluorescence, Phys. Rev. Lett. **39**, 691 (1977).
[36] Z. Shen, Y.-L. Zhang, Y. Chen, C.-L. Zou, Y.-F. Xiao, X.-B. Zou, F.-W. Sun, G.-C. Guo, and C.-H. Dong, Experimental realization of optomechanically induced non-reciprocity, Nat. Photon. **10**, 657 (2016).
[37] J. J. A. Lin, D. Paterson, A. G. Peele, P. J. McMahon, C. T. Chantler, K. A. Nugent, B. Lai, N. Moldovan, Z. Cai, D. C. Mancini, and I. McNulty, Measurement of the spatial coherence function of undulator radiation using a phase mask, Phys. Rev. Lett. **90**, 074801 (2003).
[38] J. Chan, A. H. Safavi-Naeini, J. T. Hill, S. Meenehan, and O. Painter, Optimized optomechanical crystal cavity with acoustic radiation shield, Appl. Phys. Lett. **101**, 081115 (2012).
[39] Y. Wang, Z.-P. Shi, Z. Shen, S. Wan, P.-Y. Wang, H.-Y. Kuang, G.-T. Xu, C.-L. Zou, G.-C. Guo, and C.-H. Dong, Realization of the quantum ground state in an optomechanical crystal cavity, Sci. China: Phys., Mech. Astron. **66**, 124213 (2023).
[40] S. M. Meenehan, J. D. Cohen, S. Gröblacher, J. T. Hill, A. H. Safavi-Naeini, M. Aspelmeyer, and O. Painter, Silicon optomechanical crystal resonator at millikelvin temperatures, Phys. Rev. A **90**, 011803(R) (2014).
[41] S. M. Meenehan, J. D. Cohen, G. S. MacCabe, F. Marsili, M. D. Shaw, and O. Painter, Pulsed excitation dynamics of an optomechanical crystal resonator near its quantum ground state of motion, Phys. Rev. X **5**, 041002 (2015).
[42] J. D. Cohen, S. M. Meenehan, G. S. MacCabe, S. Gröblacher, A. H. Safavi-Naeini, F. Marsili, M. D. Shaw, and O. Painter, Phonon counting and intensity interferometry of a nanomechanical resonator, Nature (London) **520**, 522 (2015).
[43] R. Riedinger, S. Hong, R. A. Norte, J. A. Slater, J. Shang, A. G. Krause, V. Anant, M. Aspelmeyer, and S. Gröblacher, Non-classical correlations between single photons and phonons from a mechanical oscillator, Nature (London) **530**, 313 (2016).
[44] J. D. Teufel, T. Donner, D. Li, J. W. Harlow, M. Allman, K. Cicak, A. J. Sirois, J. D. Whittaker, K. W. Lehnert, and R. W. Simmonds, Sideband cooling of micromechanical motion to the quantum ground state, Nature (London) **475**, 359 (2011).
[45] M. Forsch, R. Stockill, A. Wallucks, I. Marinkovic, C. Gartner, R. A. Norte, F. W. M. Van Otten, A. Fiore, K. Srinivasan, and S. Groblacher, Microwave-to-optics conversion using a mechanical oscillator in its quantum ground state, Nat. Phys. **16**, 69 (2020).
[46] A. H. Safavi-Naeini, J. Chan, J. T. Hill, T. P. M. Alegre, A. Krause, and O. Painter, Observation of quantum motion of a nanomechanical resonator, Phys. Rev. Lett. **108**, 033602 (2012).